Raman scattering in the diluted magnetic semiconductor $Zn_{1-x}Fe_xTe$: A van Vleck paramagnet

X. Lu, I. Miotkowski, A. K. Ramdas, and S. Rodriguez
Department of Physics, Purdue University, West Lafayette, Indiana 47907, USA

H. Alawadhi
Department of Applied Physics, University of Sharjah, United Arab Emirates

T. M. Pekarek
Department of Chemistry and Physics, University of North Florida, Jacksonville, Florida 32224, USA
(Received 25 February 2007; revised manuscript received 17 June 2007; published 19 July 2007)

$Zn_{1-x}Fe_xTe$, a zinc blende II-VI diluted magnetic semiconductor (DMS), exhibits a temperature independent magnetization at low temperature (van Vleck paramagnetism) as a consequence of the electronic structure of Fe^{2+} in its site symmetry as an isoelectronic replacement of Zn^{2+}. The lowest level of its $^5\Gamma_3$ ground state multiplet has a Γ_1 nonmagnetic level, with a Γ_4 magnetic level 2.26 meV above it. The Raman spectrum of this DMS displays the $\Gamma_1 \rightarrow \Gamma_4$ electronic transition (labeled in this paper $\Gamma_{1\rightarrow 4}$), whose Zeeman splitting is interpreted in terms of symmetry considerations and numerical calculations. The magnetic field and temperature dependence of the spin-flip Raman line (ω_{SFR}) of the donor-bound electron in $Zn_{1-x}Fe_xTe$ exhibit characteristics typical of the van Vleck paramagnetism and, in combination with magnetization measurements, yield the *s-d* exchange constant $N_0\alpha = 239.0 \pm 10$ meV. The Raman spectra also show $\Gamma_{1\rightarrow 4}$ in combination with the LO phonons of $Zn_{1-x}Fe_xTe$ as a ternary alloy with an intermediate mode behavior.

DOI: 10.1103/PhysRevB.76.035208 PACS number(s): 78.30.−j, 78.20.Ls, 78.55.Et

I. INTRODUCTION

Investigations on the II-VI diluted magnetic semiconductors (DMSs) to date have predominantly focused on those based on Mn; the ease with which it can be incorporated over a large concentration range (e.g., $0 \leqslant x \leqslant 0.77$ in $Cd_{1-x}Mn_xTe$), on the one hand, and the simplicity of the "atomic like"[1] $^6S_{5/2}$ ground state of Mn^{2+} substituting for Cd^{2+}, on the other, are the factors which make them attractive for a variety of magneto-optical studies. In these DMSs, Mn^{2+}, with $S=5/2$, $L=0$ and a magnetic moment of $5.92\mu_B$, displays paramagnetism which follows the $B_{5/2}$ Brillouin function. The magnetic properties of Mn-based DMSs manifested in their paramagnetism, the spin-glass and antiferromagnetic phases for large x, the associated collective excitations (magnons), as well as in their magneto-optic effects such as excitonic Zeeman effect, Faraday rotation, and spin-flip Raman scattering (SFRS), have been intensively investigated.[2] Other examples of transition metal ion (TMI)-based DMSs which show Brillouin-type paramagnetism are Co^{2+} and V^{2+}. The electronic configuration of Co^{2+} is $3d^7$ and the ground state of the free ion is $^4F_{9/2}$; Co^{2+} in $Cd_{1-x}Co_xTe$ (Ref. 3) shows an effective spin of $(3/2)\hbar$ and hence a $B_{3/2}$ Brillouin-type paramagnetism. Tsoi *et al.*[4] showed that V^{2+} in CdTe also displays a $B_{3/2}$ behavior. The magnetism of Fe^{2+} in the DMS ternaries is distinctly different from those containing Mn^{2+} and Co^{2+}. The ground state of Fe^{2+} is Γ_1, a nondegenerate level; hence, Fe^{2+}-based DMSs have no permanent magnetic moment in the absence of a magnetic field. However, the Γ_1 state mixes with the higher lying energy levels in the presence of the magnetic field, leading to an induced magnetic moment. Fe^{2+}-based DMSs therefore display a magnetic susceptibility with signatures of the type first identified by van Vleck,[5] and such crystals are said to display van Vleck-type paramagnetism. They have been investigated theoretically[6–9] as well as experimentally, with magnetic susceptibility,[10] near and far infrared spectroscopies[11–13] and Raman spectroscopy.[14–18]

In the present paper, we report the Zeeman effect of the Raman transition in $Zn_{1-x}Fe_xTe$ from the Γ_1 ground state to the Γ_4, the first excited state of the internal levels of Fe^{2+}, as a function of magnetic field B and crystallographic orientation. We also report and discuss the $\Gamma_1 \rightarrow \Gamma_4$ electronic Raman line observed in combination with the zone center longitudinal optical (LO) phonon and its overtone (2LO) for small x; with large x, the $Zn_{1-x}Fe_xTe$ as a ternary displays an intermediate mode behavior (see, e.g., Ref. 19) permitting the occurrence of $\Gamma_1 \rightarrow \Gamma_4$ in combination with "ZnTe-like" LO_1 and "FeTe-like" LO_2. Lastly, spin-flip Raman scattering from donor-bound electrons in $Zn_{1-x}Fe_xTe$ is reported and its magnetic field dependence is interpreted in the context of the van Vleck paramagnetism of Fe^{2+} in terms of magnetization measurements carried out on the same samples. These investigations complement the papers on $Cd_{1-x}Fe_xTe$ by Tsoi *et al.*[18] and by Testelin *et al.*,[20] as well as those on $Cd_{1-x}Fe_xSe$ by Heiman *et al.*[21] and by Scalbert *et al.*[22]

II. EXPERIMENT

$Zn_{1-x}Fe_xTe$ samples were grown by the modified vertical Bridgman method with nominal x values in the range from 5×10^{-5} to 0.05. Crystallographic directions along [001], [110], and [111] in the $(1\bar{1}0)$ plane were identified using x rays with Laue pictures. Resonance Raman scattering studies were performed on the $(1\bar{1}0)$ cleaved surface either in the back- or the pseudo-90°-scattering configuration shown in Fig. 1. The Raman spectra were excited with the 5145 Å line

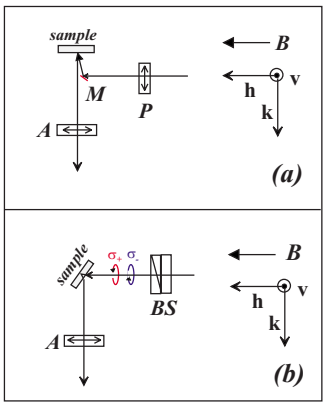

FIG. 1. (Color online) Schematical diagram for Raman measurements: (a) backscattering configuration and (b) pseudo-90°-scattering configuration. (BS) Babinet-Soleil compensator, (P) linear polarizer, (A) linear analyzer, and (M) mirror.

of an Ar^+ laser or the 5208 Å line of a Kr^+ laser, or by using tunable monochromatic radiation from a dye laser with Coumarin 7 as the dye. A superconducting optical magnetic cryostat was employed for applying magnetic fields up to 6 T and for achieving temperatures as low as 1.8 K. The scattered radiation was analyzed with a double grating spectrometer with a third grating used in tandem for a more rigorous rejection of parasitic radiation when required, and detected by standard photon-counting electronics. Wavelength-modulated reflectivity spectra were obtained at low temperatures in zero magnetic field. Magnetization measurements were performed in a magnetic field up to 7 T, employing a Quantum Design MPMS XL7 superconducing quantum interference device magnetometer, the magnetic field being perpendicular to the cleaved surfaces.

III. RESULTS AND DISCUSSION

The electronic configuration of Fe^{2+} is $3d^6$, whose lowest term is ^5D ($L=2, S=2$). As shown in Fig. 2, in a crystal of T_d symmetry, the ^5D term splits into an orbital doublet $^5\Gamma_3$ and a higher orbital triplet $^5\Gamma_5$, separated by Δ; the tenfold $^5\Gamma_3$ state is further split by the spin-orbit interaction into Γ_1, Γ_4, Γ_3, Γ_5, and Γ_2 levels in order of increasing energy.[6] The Raman active $\Gamma_1 \rightarrow \Gamma_4$ internal transition of Fe^{2+} has been investigated in the present study in the context of its role in the van Vleck paramagnetism displayed by Fe-based DMSs.

Several $Zn_{1-x}Fe_xTe$ samples with differing iron concentrations were characterized with "wavelength modulated reflectivity (WMR)," as shown in Fig. 3. The energy shifts of the excitonic band gap relative to pure ZnTe range from 0.9 to 10 meV, indicating that the specimens are indeed ternary alloys. From the calibration curve established by Testelin *et al.*[23] for the excitonic energy as a function of x determined from x-ray fluorescence, i.e., $E_{gx}(x)=2379+1200x$ (meV), we deduce the values of x for the four specimens employed in Fig. 3 to be 7.5×10^{-4}, 2.5×10^{-3}, 6.3×10^{-3}, and 8.3×10^{-3}.

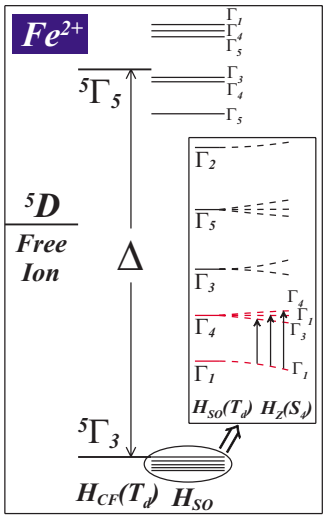

FIG. 2. (Color online) Schematic diagram of the energy levels of Fe^{2+} in a tetrahedral crystal field ($\hat{H}_{CF}$), the spin-orbit interaction ($\hat{H}_{SO}=\lambda \mathbf{L}\cdot\mathbf{S}$), and Zeeman energy ($\hat{H}_Z$) in an external magnetic field. We assume that $\hat{H}_{CF} > \hat{H}_{SO} > \hat{H}_Z$.

A. $\Gamma_1 \rightarrow \Gamma_4$ electronic Raman transition and its combination with longitudinal optical phonons: $B=0$

The Raman spectrum of $Zn_{1-x}Fe_xTe$ with $x=7.5\times10^{-4}$, excited by the 5145 Å Ar^+ line (with a power of ~30 mW) in the backscattering configuration, is shown in Fig. 4. At 10 K, the Raman lines associated with the $\Gamma_1 \rightarrow \Gamma_4$ internal transition (labeled as $\Gamma_{1\rightarrow4}$ hereafter), TO and LO phonons occur with shifts of 18.2, 181.5, and 211 cm^{-1}, respectively. The LO phonon shifted 1 cm^{-1} higher than that of ZnTe at 210 cm^{-1}. The Raman shift of $\Gamma_{1\rightarrow4}$ at 18.2 cm^{-1} is consis-

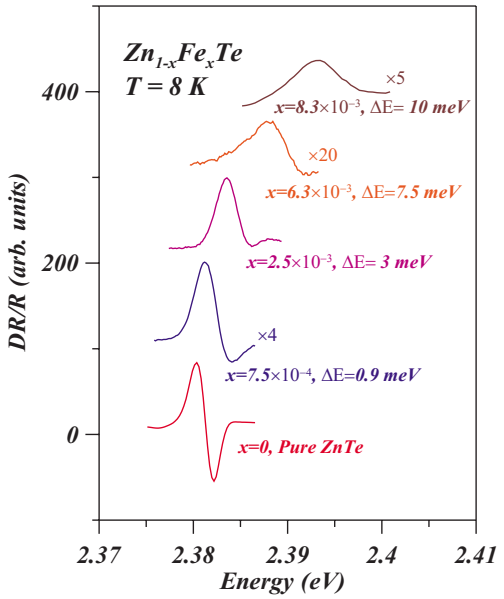

FIG. 3. (Color online) Wavelength modulation reflectivity (WMR) spectra of $Zn_{1-x}Fe_xTe$ showing the excitonic band gap shift (ΔE) as a function of x referred to that of pure ZnTe.

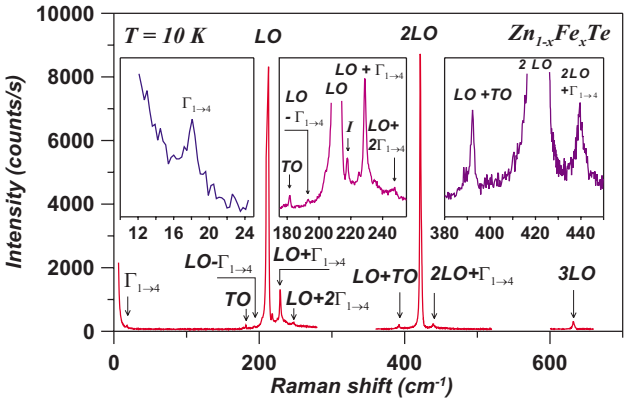

FIG. 4. (Color online) Raman spectrum of $\Gamma_{1\to4}\equiv\Gamma_1\to\Gamma_4$, $LO\pm\Gamma_{1\to4}$, $LO+2\Gamma_{1\to4}$, and $2LO+\Gamma_{1\to4}$ for $Zn_{1-x}Fe_xTe$ ($x=0.075\%$) at $T=10$ K, excited by 5145 Å (30 mW) line from an Ar^+ laser.

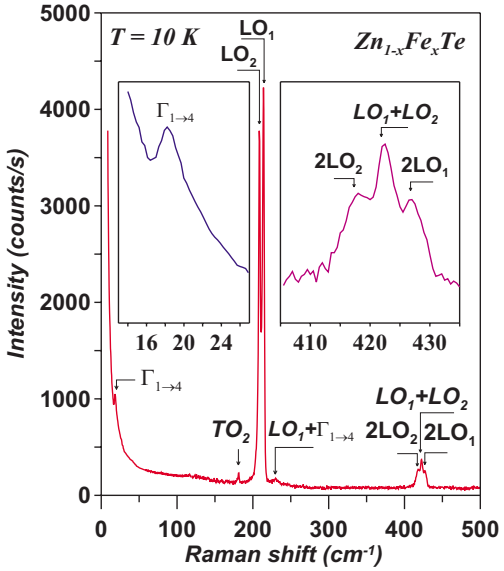

FIG. 5. (Color online) Raman spectrum of $Zn_{1-x}Fe_xTe$ ($x\sim0.01$) showing intermediate mode behavior. $LO_1\equiv LO(ZnTe)$, $LO_2\equiv LO(FeTe)$, and $\lambda_L=5145$ Å line from Ar^+ laser and $T=10$ K.

tent with that reported by Jouanne *et al.*[17] In addition, the Raman spectrum shows features with shifts of $LO\pm\Gamma_{1\to4}$, $LO+2\Gamma_{1\to4}$, and $2LO+\Gamma_{1\to4}$ at 193.1, 229, 247.7, and 440 cm^{-1}, respectively. The feature denoted with I in the figure appears to be due to LO+I, associated with an unidentified impurity. Following Mauger *et al.*,[8] the virtual transitions responsible for the $\Gamma_{1\to4}$ Raman lines of Fe^{2+} in $Zn_{1-x}Fe_xTe$ have their origin in the Heisenberg-type exciton-ion exchange interaction given by

$$\hat{H}_{ex}=-(\alpha\mathbf{S}_e+\beta\mathbf{S}_h)\cdot\mathbf{S}, \tag{1}$$

where $\mathbf{S}_e$, $\mathbf{S}_h$, and $\mathbf{S}$ denote spin operators of electron, hole, and Fe^{2+} ion, respectively; α and β are the corresponding exchange constants. The Raman scattering associated with $\Gamma_{1\to4}$ is visualized as a three-step sequence of virtual transition process:[17] (i) an incident photon with energy E_i is absorbed and an exciton in the intermediate state X_μ is created, (ii) the Fe^{2+} ion is then excited from Γ_1 to Γ_4 through exciton-Fe^{2+} exchange interaction in which the exciton is transferred from state X_μ to X_ν, and (iii) the exciton recombines to emit a scattered photon with energy $E_i\pm E_{\Gamma_{1\to4}}$. The $LO\pm\Gamma_{1\to4}$ Raman transitions are the combination of LO phonon with $\Gamma_{1\to4}$ through the Fröhlich interaction. $LO+\Gamma_{1\to4}$ involves the creation of an LO phonon as well as $\Gamma_{1\to4}$, whereas $LO-\Gamma_{1\to4}$ corresponds to the creation of an LO phonon and the deexcitation of Fe^{2+} from Γ_4 to Γ_1. Since the same Fe^{2+} ion cannot make two successive $\Gamma_{1\to4}$ excitations, the microscopic process for $LO+2\Gamma_{1\to4}$ must involve multiple iron ions such as $Fe^{2+}-Fe^{2+}$ pairs. Due to the extended nature of the excitonic wave function, one can visualize an exciton interacting with several Fe^{2+} ions at the same time.

Raman spectrum of a sample with a significantly higher x ($x\sim0.01$), recorded at 10 K, is shown in Fig. 5. In addition to $\Gamma_{1\to4}$, one can observe many phonon features characteristic of $Zn_{1-x}Fe_xTe$ as a ternary, viz., ZnTe-like LO_1 at 213.7 cm^{-1} shifted to a higher frequency by 3.7 cm^{-1}, compared to the LO mode frequency of pure ZnTe at 210 cm^{-1}; ZnTe-like TO_2 at 181.5 cm^{-1}; FeTe-like LO_2 (or the band mode ZnTe:Fe) at 209 cm^{-1}; $LO_1+\Gamma_{1\to4}$ at 231.9 cm^{-1}; $2LO_1$ at 427.4 cm^{-1}, $2LO_2$ at 418 cm^{-1}; and LO_1+LO_2 at 422.7 cm^{-1}. The many phonon features in Fig. 5 can be understood better by comparing them to the vibrational modes in $Zn_{1-x}Mn_xTe$,[19] $Zn_{1-x}Fe_xSe$,[24] and $Zn_{1-x}Co_xSe$,[24] which all show what is called the intermediate mode behavior. With the evidence that the ZnTe-like LO_1 shifts to higher frequencies with increasing x, and given the small mass difference between Fe and Mn (or Co), we believe that $Zn_{1-x}Fe_xTe$ also shows an intermediate mode behavior. In contrast, the vibrational modes in $Cd_{1-x}Mn_xTe$ exhibit what is known as the two-mode behavior.[19,25] Although the resonance Raman scattering has allowed the observation of the many phonon features even at very low iron concentrations ($x\sim0.01$) in $Zn_{1-x}Fe_xTe$, one needs much higher x to explore the concentration dependence of the phonon frequencies to fully establish the intermediate mode behavior.

B. Zeeman effect of $\Gamma_{1\to4}$

The Zeeman effect of the $\Gamma_{1\to4}$ Raman transition is presented in this section. The Raman spectra excited with the 5208 Å Kr^+ line were recorded with $B\|[100]$, [110], or [111] in the backscattering configuration, as shown in Fig. 6 for $Zn_{1-x}Fe_xTe$ ($x=7.5\times10^{-4}$). In Fig. 7, the Raman shifts of the Zeeman components as a function of B along different crystallographic directions (circular solid dots) are compared with theoretical calculations (solid line). The theoretical study makes use of the Hamiltonian

$$\hat{H}=\hat{H}_0+\hat{H}_{CF}+\hat{H}_{SO}+\hat{H}_Z, \tag{2}$$

where $\hat{H}_0$ is the Hamiltonian of the free Fe^{2+} excluding the spin-orbit coupling, $\hat{H}_{CF}$ is the crystal field Hamiltonian (de-

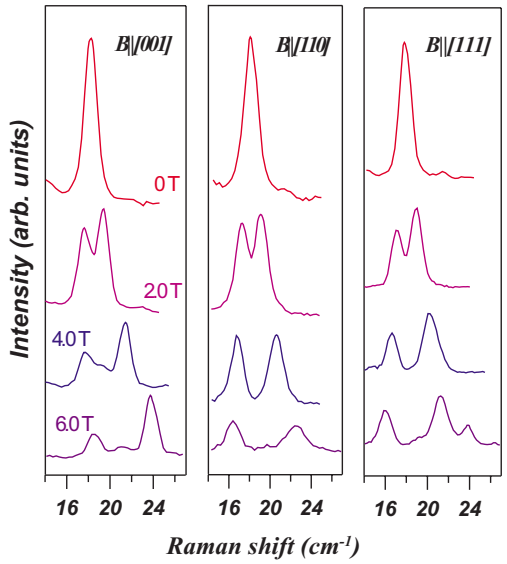

FIG. 6. (Color online) The magnetic field dependence of the Zeeman components of the $\Gamma_{1\to4}$ Raman transition of Fe^{2+} along [001], [011], or [111].

noting the energy separation between $^5\Gamma_5$ and $^5\Gamma_3$ by Δ), $\hat{H}_{SO}=\lambda\mathbf{L}\cdot\mathbf{S}$ is the spin-orbit interaction, and $\hat{H}_Z=\mu_B\mathbf{B}\cdot(\mathbf{L}+2\mathbf{S})$ is the Zeeman interaction. The manifold of the 25 wave functions of the free ^5D ground term states ($S=2$, $L=2$) is chosen as a complete basis set and the 25×25 matrix under the Hamiltonian $\hat{H}$ was calculated. The eigenvalues and the eigenfunctions of the matrix are solved numerically by choosing the two parameters λ and Δ such that the zero-field Raman shift $\Gamma_{1\to4}$ equals 18.2 cm^{-1} (from this measurement)

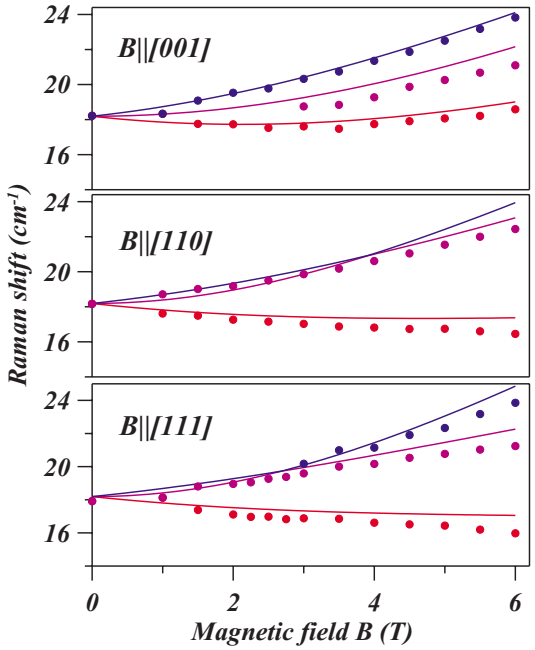

FIG. 7. (Color online) The experimental results of $\Gamma_{1\to4}$ (circular dots) compared with the numerical calculations (solid line) with $\mathbf{B}\|[001]$, [110], or [111].

and the infrared transition Γ_1 (belonging to $^5\Gamma_3$) $\to\Gamma_5$ (belonging to $^5\Gamma_5$), as shown in Fig. 2, equals 2486 cm^{-1} (see Ref. 26). The values for $\lambda=-102.2$ cm^{-1} and $\Delta=2693$ cm^{-1} deduced here are exactly the same as those reported by Testelin *et al.*[23]

The presence of the magnetic field reduces the T_d site symmetry of Fe^{2+} to S_4, C_s, and C_3 for $B\|[100]$, [110], and [111], respectively,[27] the corresponding decomposition of $\Gamma_4(T_d)$ being given by $\Gamma_1+\Gamma_3+\Gamma_4$ in S_4, $\Gamma_1+2\Gamma_2$ in C_s, and $\Gamma_1+\Gamma_2+\Gamma_3$ in C_3. Our numerical calculations of the eigenvalues and eigenfunctions for the $\Gamma_{1\to4}$ transition of Fe^{2+} in the presence of the magnetic field are consistent with the group theoretical analysis. The Zeeman components in the order of increasing energy, as shown in Fig. 7, belong to Γ_3, Γ_1, Γ_4 for $B\|[001]$, Γ_2, Γ_1, Γ_2 for $B\|[110]$, and Γ_2, Γ_3, Γ_1 for $B\|[111]$.

The Raman tensors characterizing $\Gamma_{1\to4}$ obtained using group theory are given in Eqs. (1)–(3) of Tsoi *et al.*[18] The selection rules based on them are presented in Table I. Backscattering and pseudo-90°-scattering configurations employed for checking the rules are schematically depicted in Fig. 1. A right-hand laboratory coordinate system $(\mathbf{k},\mathbf{h},\mathbf{v})$ has been used, the magnetic field $\mathbf{B}$ is fixed along the horizontal $(\mathbf{h})$ direction, and the scattered light propagates along the $\mathbf{k}$ direction. For backscattering geometry [Fig. 1(a)], the incident light propagates along $\bar{\mathbf{k}}$ with polarization along $\mathbf{v}$ or $\mathbf{h}$ and the scattered light was analyzed along $\mathbf{h}$, which results in $\bar{\mathbf{k}}(\mathbf{vh})\mathbf{k}$ and $\bar{\mathbf{k}}(\mathbf{hh})\mathbf{k}$ polarization configurations. For pseudo-90°-scattering configuration [Fig. 1(b)], the incident light propagates along $\mathbf{h}$ with σ_+ and σ_- polarizations and the scattered light was analyzed along $\mathbf{h}$, which results in $\mathbf{h}(\sigma_+,\mathbf{h})\mathbf{k}$ and $\mathbf{h}(\sigma_-,\mathbf{h})\mathbf{k}$ polarization configurations.

The Zeeman components of $\Gamma_{1\to4}$ observed in the Raman spectra for the different polarization configurations are shown in Fig. 8, recorded at 5 K and 6 T. The appearance of scattered light not allowed in the specific configurations can be attributed to several factors. (1) In $\mathbf{h}(\sigma_+,\mathbf{h})\mathbf{k}$ and $\mathbf{h}(\sigma_-,\mathbf{h})\mathbf{k}$ configurations, the exciting radiation is very close to the excitonic transitions but results in a very shallow penetration depth. Although essential for resonance enhancement, the scattering is then restricted to a very small volume in the exact 90° scattering; thus, one has to tilt the sample and use "pseudo-90°-scattering" for obtaining reasonable scattering intensity and accept the limitations of the departure from the exact 90° scattering geometry. (2) In both back- and pseudo-90°-scattering geometries, the finite solid angle essential for collecting the scattered light results in "leakage" of light in the undesired direction and in turn a degradation in the selection rule. (3) The linear polarizers with a sufficiently large aperture, e.g., polaroids, are not perfect. They too contribute to the leakage into the forbidden geometry. (4) Finally, in resonance Raman scattering, forbidden Raman features may appear under resonant enhancement, as shown, for example, in Ref. 28. To summarize, the strict exclusion expected in the polarization configurations is only partially realized but nevertheless is qualitively consistent with the selection rules. By comparing Table I and Fig. 8, the relative intensities for the different peaks under different polarization configurations allow one to distinguish and assign different peaks.

TABLE I. Selection rules for the Zeeman components of $\Gamma_{1\to4}$ in the presence of an external magnetic field **B** along [001], [110], or [111].

		$\bar{\mathbf{k}}(\mathbf{vh})\mathbf{k}$	$\bar{\mathbf{k}}(\mathbf{hh})\mathbf{k}$	$\mathbf{h}(\sigma_-,\mathbf{h})\mathbf{k}$	$\mathbf{h}(\sigma_+,\mathbf{h})\mathbf{k}$
$\mathbf{B}\|[001]$	$\Gamma_1\to\Gamma_1$	No	Yes	No	No
	$\Gamma_1\to\Gamma_3$	Yes	No	Yes	No
	$\Gamma_1\to\Gamma_4$	Yes	No	No	Yes
$\mathbf{B}\|[110]$	$\Gamma_1\to\Gamma_1$	No	Yes		
	$\Gamma_1\to\Gamma_2$	Yes	No		
$\mathbf{B}\|[111]$	$\Gamma_1\to\Gamma_1$	No	Yes	No	No
	$\Gamma_1\to\Gamma_2$	Yes	No	Yes	No
	$\Gamma_1\to\Gamma_3$	Yes	No	No	Yes

For $B\|[100]$, as shown in Fig. 8(a), (i) $\Gamma_1\to\Gamma_1$ appears only in $\bar{\mathbf{k}}(\mathbf{hh})\mathbf{k}$, (ii) $\Gamma_1\to\Gamma_3$ in $\mathbf{h}(\sigma_-,\mathbf{h})\mathbf{k}$ is stronger than in $\mathbf{h}(\sigma_+,\mathbf{h})\mathbf{k}$, and (iii) $\Gamma_1\to\Gamma_4$ in $\mathbf{h}(\sigma_+,\mathbf{h})\mathbf{k}$ is stronger than in $\mathbf{h}(\sigma_-,\mathbf{h})\mathbf{k}$. The combination of the above three spectra allows one to identify $\Gamma_1\to\Gamma_1$, Γ_3, or Γ_4. For $B\|[011]$, Fig. 8(b) shows two peaks in $\bar{\mathbf{k}}(\mathbf{vh})\mathbf{k}$, which correspond to the two allowed $\Gamma_1\to\Gamma_2$ transitions since the separation between Γ_1 and the higher energy level Γ_2 is so small that the transition $\Gamma_1\to\Gamma_1$ merges with the transition $\Gamma_1\to\Gamma_2$ (see Fig. 7), preventing the observation of $\Gamma_1\to\Gamma_1$ as a well resolved Raman line. The identification for $B\|[111]$ shown in Fig. 8(c) is similar to that for $B\|[001]$: (i) $\Gamma_1\to\Gamma_3$ in $\mathbf{h}(\sigma_+,\mathbf{h})\mathbf{k}$ is stronger than in $\mathbf{h}(\sigma_-,\mathbf{h})\mathbf{k}$, (ii) $\Gamma_1\to\Gamma_2$ in $\mathbf{h}(\sigma_-,\mathbf{h})\mathbf{k}$ is stronger than in $\mathbf{h}(\sigma_+,\mathbf{h})\mathbf{k}$, and (iii) the relative intensity of $\Gamma_1\to\Gamma_1$ with respect to those of $\Gamma_1\to\Gamma_3$ and $\Gamma_1\to\Gamma_2$ in $\bar{\mathbf{k}}(\mathbf{hh})\mathbf{k}$ is much bigger than in $\bar{\mathbf{k}}(\mathbf{vh})\mathbf{k}$.

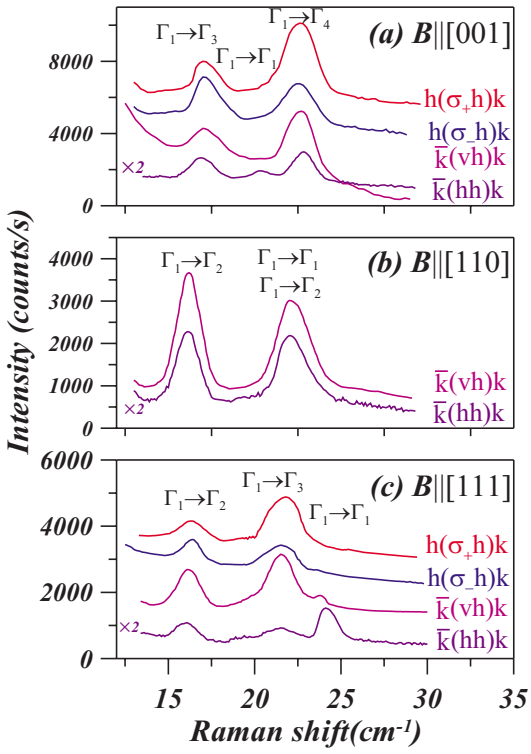

FIG. 8. (Color online) Zeeman components of the $\Gamma_1\to\Gamma_4$ Raman transition of Fe^{2+}, recorded at $T=5$ K and $B=6$ T in different polarization configurations for magnetic field along (a) [001], (b) [110], or (c) [111].

C. Paramagnetism of Fe^{2+} in a tetrahedral environment

In order to explore the microscopic mechanism underlying the van Vleck paramagnetism more physically, it is useful to deduce analytical expressions under specific approximations, although numerical calculations presented in Sec. III B provide more accurate results over a wider range of temperature and magnetic field.

In this section, we describe the magnetic behavior of a single Fe^{2+} ion in a strong crystal field of symmetry T_d (i.e., $\hat{H}_{CF}\gg\hat{H}_{SO}$). In Fig. 2, we have displayed the energy level scheme obtained in the absence of the spin-orbit interaction on the left-hand side of the diagram. The orbital D states split into a triplet Γ_5 and a doublet Γ_3, the former lying at an energy Δ above the latter. We label the eigenvectors thus obtained with Greek letters following the usage of von der Lage and Bethe.[29] Thus, Γ_3 levels are denoted by γ_i $(i=1,2)$ and Γ_5 states by ϵ_i $(i=1,2,3)$. The $|M_L\rangle$ states for $L=2$ $(M_L=2,1,0,-1,-2)$ are selected so that $\gamma_{1,2}$ transform under the operations of T_d as $(2z^2-x^2-y^2)$ and $\sqrt{3}(x^2-y^2)$ or $\gamma_1=|0\rangle$ while $\gamma_2=(1/\sqrt{2})(|2\rangle+|-2\rangle)$. In an analogous way, the orbital Γ_5 states transform as yz, zx, and xy and are $\epsilon_1=(i/\sqrt{2})(|1\rangle+|-1\rangle)$, $\epsilon_2=(1/\sqrt{2})(-|1\rangle+|-1\rangle)$, and $\epsilon_3=(i/\sqrt{2})\times(-|2\rangle+|-2\rangle)$. The axes x, y, and z are the cubic axes of the host crystal. To include the effect of spin-orbit interaction, displayed on the right-hand side of Fig. 2, we consider the vectors $|M_S\rangle$ of the $S=2$ spin of the ^5D configuration of Fe^{2+}. The $^5\Gamma_3$ states of the lower multiplet, tenfold degenerate in the absence of $\hat{H}_{SO}$, separate into the five levels Γ_1, Γ_4, Γ_3, Γ_5, and Γ_2 given in the order of increasing energy. The lowest state being a singlet is nonmagnetic but Γ_4, connected to Γ_1 by the Zeeman interaction at very low temperatures, gives rise to a temperature independent magnetization, i.e., van Vleck paramagnetism. In order to describe this mixing, we introduce symmetry-adapted spin states, denoted again by

Greek letters, using the convention employed for the orbital states except that they are distinguished from the orbital states by a tilde, i.e., by $\tilde{\gamma}_i$ $(i=1,2)$, $\tilde{\epsilon}_i$ $(i=1,2,3)$, etc. The Γ_1 and Γ_4 states of the ${}^5\Gamma_3$ multiplet are $|\alpha\rangle=(1/\sqrt{2})(\gamma_1\tilde{\gamma}_1+\gamma_2\tilde{\gamma}_2)$ and $|\delta_1\rangle=(-1/2)(\sqrt{3}\gamma_1+\gamma_2)\tilde{\epsilon}_1$, and $|\delta_2\rangle=(1/2)(\sqrt{3}\gamma_1-\gamma_2)\tilde{\epsilon}_2$ and $|\delta_3\rangle=\gamma_2\tilde{\epsilon}_3$. The complete set of symmetry-adapted vectors are given in the Tables 1 and 2 of Colignon *et al.*[30] Taking into account the coupling with the ${}^5\Gamma_5$ states caused by the spin-orbit interaction, the $|\alpha\rangle$ and $|\delta_i\rangle$ states become, to the first order in (λ/Δ), $|\Phi_\alpha\rangle=|\alpha\rangle+|\alpha'\rangle(2\sqrt{6}\lambda/\Delta)$ and $|\Phi_{\delta_i}\rangle=|\delta_i\rangle-|\delta_i'\rangle(\sqrt{6}\lambda/\Delta)+|\delta_i''\rangle(2\sqrt{3}\lambda/\Delta)$ $(i=1,2,3)$, where $|\alpha'\rangle$, $|\delta_i'\rangle$, and $|\delta_i''\rangle$ denote vectors in the ${}^5\Gamma_5$ multiplet. To second order in (λ/Δ), the energy eigenvalues of $|\Phi_\alpha\rangle$ and $|\Phi_{\delta_i}\rangle$ are $E_\alpha=-(24\lambda^2/\Delta)(1+2\lambda/\Delta)$ and $E_\delta=-(18\lambda^2/\Delta)(1+\lambda/\Delta)$, giving $W=E_\delta-E_\alpha=E_{1\to4}=(6\lambda^2/\Delta)(1+5\lambda/\Delta)$. With $\lambda=-102.2$ cm^{-1} and $\Delta=2693$ cm^{-1} from the numerical calculation, we obtain $W=18.86$ cm^{-1} in reasonable agreement with the observed value of 18.2 cm^{-1}.

The Zeeman interaction mixes $|\Phi_\alpha\rangle$ and $|\Phi_{\delta_i}\rangle$; taking the magnetic field along one of the cubic axes, say, z, the only nonvanishing matrix elements of $\hat{H}_Z$ are

$$\langle\Phi_\alpha|\mu_B B(L_z+2S_z)|\Phi_{\delta_3}\rangle=-2i\sqrt{2}(1-4\lambda/\Delta)\mu_B B \qquad (3)$$

and

$$\langle\Phi_{\delta_1}|\mu_B B(L_z+2S_z)|\Phi_{\delta_2}\rangle=-i(1+2\lambda/\Delta)\mu_B B. \qquad (4)$$

To the lowest terms in B, the eigenvalues of the 4×4 submatrix $\hat{H}_Z$ in $(\Phi_\alpha,\Phi_{\delta_i})$ are $[-8(\mu_B B)^2/W](1-4\lambda/\Delta)^2$, $W+[8(\mu_B B)^2/W](1-4\lambda/\Delta)^2$, and $W\pm\mu_B B(1+2\lambda/\Delta)$. At temperature T, the occupation probabilities with $4\mu_B B\ll W$ are $[1+3e^{-W/(k_BT)}]^{-1}$ and $e^{-W/(k_BT)}[1+3e^{-W/(k_BT)}]^{-1}$ for Γ_1 and Γ_4, respectively, so that for $W\gg k_BT$, the expectation value of the magnetic moment is

$$\overline{\langle\mu_z\rangle}=\frac{16\mu_B^2 B}{W}\left(1-\frac{4\lambda}{\Delta}\right)^2. \qquad (5)$$

When $W\ll k_BT$, the states $|\delta_1\rangle$ and $|\delta_2\rangle$ do not contribute significantly to the magnetization and

$$\overline{\langle\mu_z\rangle}=\frac{4\mu_B^2 B}{k_BT}\left(1-\frac{4\lambda}{\Delta}\right)^2. \qquad (6)$$

At extremely high magnetic fields at low temperature, the ${}^5\Gamma_3$ states can be considered as degenerate $(\mu_B B\gg W)$ and the saturation magnetization is $4\mu_B(1-4\lambda/\Delta)$.

Using $\lambda=-102.2$ cm^{-1} and $\Delta=2693$ cm^{-1} for Fe^{2+} in ZnTe, we obtain, at zero temperature, $\overline{\langle\mu_z\rangle}=0.54\mu_B$B and the saturation value as $B\to\infty$ is $4\mu_B(1-4\lambda/\Delta)=4.61\mu_B$. In the linear approximation, $\overline{\langle\mu_z\rangle}$ is independent of the direction of the magnetic field with respect to the crystal axes. However, a glance at Fig. 7 clearly shows that this is not true when the nonlinear terms in the magnetization become important. The reason for the energy anisotropy as a function of **B** and, hence, of the Raman line $\Gamma_{1\to4}$, arises because the Zeeman interaction not only mixes Γ_1 and Γ_4 but also Γ_4 and Γ_3 when **B** is along a cubic axis and Γ_4 and Γ_5 which in turn mix with Γ_2 when **B** is along [111] (see Ref. 7).

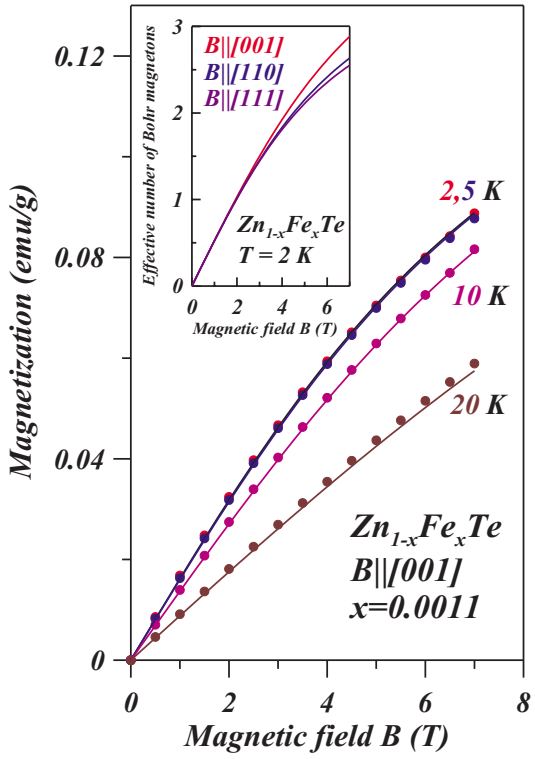

FIG. 9. (Color online) Experimental magnetization data (dots), after subtracting the diamagnetic contribution of the host and fitted with the numerically calculated curve (solid lines), yields $x=1.1\times10^{-3}$. The numerically calculated values of the effective number of Bohr magnetons shown in the inset display anisotropy with $B\|[001]$, [110], and [111].

In general, to analyze the above results, it is more convenient to calculate numerically the magnetization using the totality of the ${}^5D$ states. The corresponding diagonalization of the 25×25 matrix yields results which agree with the low field calculation given here. The macroscopic magnetization can thus be calculated in terms of $\overline{\langle\mu_z\rangle}$, $M_m^*=[xN_A/W_m(x)]\overline{\langle\mu_z\rangle}$, where N_A is the Avogadro's number and $W_m(x)$ is the molar weight of $Zn_{1-x}Fe_xTe$. Figure 9 shows the experimental magnetization data after subtracting the diamagnetic contribution as well as numerically calculated results for $Zn_{1-x}Fe_xTe$; the x value $(x=1.1\times10^{-3})$ thus deduced is slightly different from that deduced using the calibration curve established by Testelin *et al.*[23] $(x=7.5\times10^{-4})$, due to the experimental errors in WMR or x-ray fluorescence measurements. In the inset of Fig. 9, the numerically calculated values of the effective number of Bohr magnetons with $B\|[001]$, [110], and [111] show the anisotropic characteristic of the van Vleck paramagnetism. Figure 10 shows the numerically calculated effective number of Bohr magnetons as a function of temperature for several magnetic fields; at low temperatures, the temperature independent characteristic of the van Vleck paramagnetism can be clearly seen.

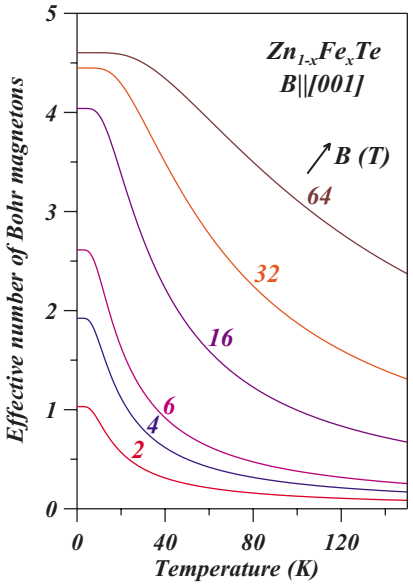

FIG. 10. (Color online) The effective number of Bohr magnetons as a function of temperature for several magnetic fields.

D. Spin-flip Raman scattering from donor-bound electrons

The strong exchange interaction between the d electrons of the TMI and the band carriers (s, p electrons) causes a huge excitonic Zeeman splitting of the DMS. Excitonic Zeeman effect observed in magnetoreflectivity yields the s-d and p-d exchange constants ($N_0\alpha$ and $N_0\beta$) in various Fe-based DMSs.[3,23,31–33] SFRS from donor-bound electrons reveals the conduction band splitting only and can be used to obtain $N_0\alpha$, as demonstrated in $Cd_{1-x}Fe_xS$,[16] $Cd_{1-x}Fe_xTe$,[18] and $Cd_{1-x}Fe_xSe$.[21] In addition, SFRS produces signatures narrower than those in unmodulated magnetoreflectivity,[23,31–33] allowing $N_0\alpha$ to be determined with a higher precision in the former than in the latter. SFRS also shows the occurrence of a bound magnetic polaron in Mn-based DMSs[34–38] as well as in van Vleck paramagnets.[15,22] In this section, we report the experimental results of SFRS in $Zn_{1-x}Fe_xTe$ and $N_0\alpha$ deduced from the combination of SFRS shifts with the magnetization measurements.

In Fig. 11, the Raman spectrum of $Zn_{1-x}Fe_xTe$ ($x=0.0025$), recorded at 2 K and 6 T and excited by the 5208 Å Kr^+ line, is displayed. The spin-flip Raman shift is given by[18,38]

$$\hbar\omega_{SFR} = g^*\mu_B B - x\alpha N_0\langle\langle S_z\rangle\rangle, \tag{7}$$

where g^* is the intrinsic g factor of the host lattice, and $\langle\langle S_z\rangle\rangle$ is the thermal and spatial average of the magnetic ion spin projection along the direction of magnetic field. The first term in Eq. (7) is the intrinsic Zeeman splitting of host crystal, and the second term is known as the s-d exchange energy, arising from the s-d exchange interaction between band electrons and the magnetic ion. $\langle\langle S_z\rangle\rangle$ can be expressed in terms of macroscopic magnetization M_m^*,[18] and Eq. (7) thus becomes

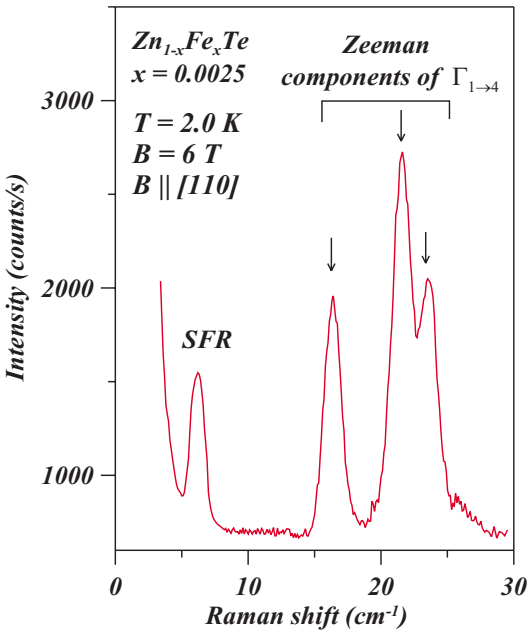

FIG. 11. (Color online) The Raman spectrum of $Zn_{1-x}Fe_xTe$ ($x=0.0025$) recorded at $T=2.0$ K and $B=6$ T. SFR is the spin-flip Raman feature from donor-bound electrons, and the left three features are associated with Zeeman components of $\Gamma_{1\to4}$ of Fe^{2+}.

$$\hbar\omega_{SFR} = g^*\mu_B B + \alpha N_0 \frac{W_m(x)}{\mu_B N_A}\frac{\langle\langle S_z\rangle\rangle}{\langle\langle L_z + 2S_z\rangle\rangle}M_m^*. \tag{8}$$

For $Zn_{1-x}Fe_xTe$, $g^*=0.42$ (see Ref. 28) and $\langle\langle L_z+2S_z\rangle\rangle/\langle\langle S_z\rangle\rangle$ equals to 2 in the lowest approximation due to the quenching of the orbital angular momentum. The quantity equals to 2.275 at $T=2$ K in the exact numerical calculation carried out using the 25 $^5D_2$ levels. This is in agreement with the value in Ref. 23. Notice that the second term in Eq. (8) has a linear relationship with respect to M_m^* and its least squares linear fit yields $N_0\alpha$.

As pointed out in Ref. 18, the observed anisotropy of the s-d exchange energy in $Cd_{1-x}Fe_xTe$ is consistent with that observed in magnetization,[20,39] which indicates that the s-d exchange constant $N_0\alpha$ in $Cd_{1-x}Fe_xTe$ is isotropic. Hence, one expects an isotropic s-d exchange constant in $Zn_{1-x}Fe_xTe$ also. The s-d exchange energy as well as the magnetization as a function of magnetic field are plotted in Fig. 12 at several temperatures, which clearly show the characteristic signatures of the van Vleck paramagnetism: (1) magnetization and s-d exchange energy show no sign of saturation at 7 T and 2 K, and (2) both magnetization and s-d exchange energy do not change, within experimental errors, as the temperature is lowered from 5 to 2 K.

In $Zn_{1-x}Fe_xTe$ alloys, except sp-d exchange interactions, another type of interaction between Fe^{2+} and Fe^{2+} is called d-d exchange interaction. This antiferromagnetic interaction must be taken into account as x increases because the nearest neighbor and next nearest neighbor d-d interaction make noticeable contributions to the magnetization. Due to the extremely small x in our present investigation, we neglect the contribution of iron clusters as Testelin *et al.*[23] did in an

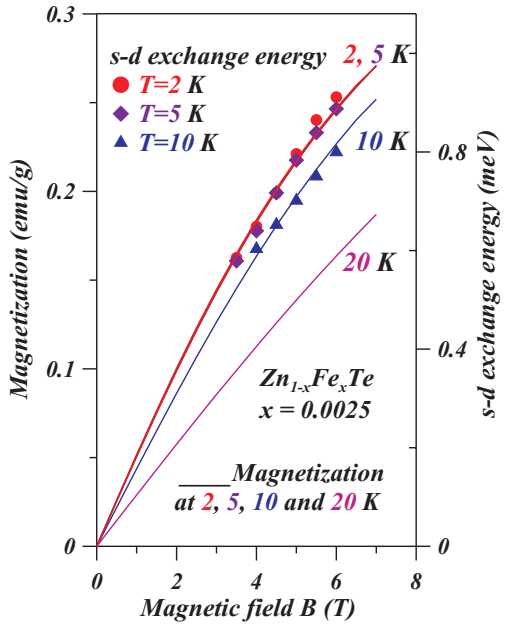

FIG. 12. (Color online) Magnetization (solid lines) corrected for the host diamagnetism as a function of magnetic field B at T=2, 5, 10, and 20 K for $Zn_{1-x}Fe_xTe$ (x=0.0025). s-d exchange energy (data points) vs B is plotted at T=2, 5, and 10 K for the same sample.

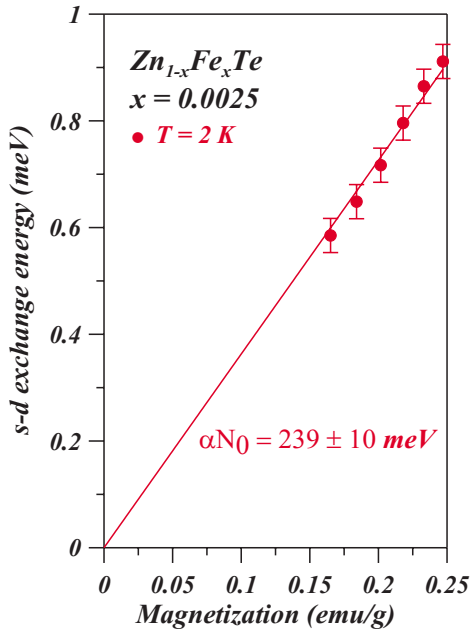

FIG. 13. (Color online) s-d exchange energy vs magnetization at T=2 K for $Zn_{1-x}Fe_xTe$ (x=0.0025). The solid line is the linear least squares fit.

earlier study. Hence, the quantity $\langle\langle L_z+2S_z\rangle\rangle/\langle\langle S_z\rangle\rangle$ takes the value for an isolated Fe^{2+} in $Zn_{1-x}Fe_xTe$. The s-d exchange energy versus magnetization at 2 K is plotted in Fig. 13 and the linear least squares fit yields the s-d exchange constant, $N_0\alpha$, to be 239±10 meV, consistent with 290±90 meV determined from the magnetoreflectivity.[23] The s-d exchange constant thus deduced is in the range of 200–300 meV, as typically observed for other II-VI DMSs.[3]

IV. CONCLUDING REMARKS

The unique van Vleck paramagnetism of Fe^{2+}, replacing the group II cations in the II-VI tetrahedrally coordinate DMSs, has been the focus of many experimental[10–18] and theoretical[6–9] studies. The electronic energy level scheme of Fe^{2+} in the II-VI DMSs of either the zinc blende or the wurtzite symmetry displays a nonmagnetic ground state with magnetic excited levels separated by W lying above it. With $W \gg k_BT$, in the presence of a magnetic field, the ground state and the excited states mix, resulting in temperature independent magnetization. With $W \ll k_BT$, the magnetization is proportional to B/T. The SFRS signatures of donor-bound electrons, mediated by s-d exchange interaction in Fe-based DMSs, also display these characteristic features of the van Vleck paramagnetism. The Zeeman effect of the $\Gamma_{1\to4}$ electronic transitions of Fe^{2+} in both $Zn_{1-x}Fe_xTe$ and $Cd_{1-x}Fe_xTe$ (Ref. 18) is satisfactorily explained in terms of symmetry considerations and numerical calculations based on crystal field, spin-orbit, and Zeeman interactions. This implies a relatively small effect of the dynamic Jahn-Teller interaction in the levels originating from the $^5\Gamma_3$ orbital doublet up to the maximum magnetic field of 6 T used in the present study. We note that $N_0\alpha$ obtained for $Zn_{1-x}Fe_xTe$, 239±10 meV, is in good agreement with 244±10 meV for $Cd_{1-x}Fe_xTe$.

The occurrence of the zone center LO phonon features in Mn- and Co-based II-VI DMSs in combination with Raman-EPR (electron paramagnetic resonance), but not or only very weakly with TO phonons,[40] has been attributed to Fröhlich interaction expected for the former. In $Zn_{1-x}Fe_xTe$, the occurrence of $\Gamma_{1\to4}$ in combination with LO and its combinations and/or overtones could well be due to the same mechanism. Of course in the van Vleck systems, one does not expect Raman-EPR. The observation of a fully delineated multimode phonon behavior in $Zn_{1-x}Fe_xTe$ ternaries would require a much higher Fe concentration, as shown by $Zn_{1-x}Mn_xTe$ (Ref. 19) and $Zn_{1-x}Fe_xSe$,[24] for example.

ACKNOWLEDGMENTS

The authors thank the National Science Foundation for support through Grant No. DMR-0405082 at Purdue University. The work carried out at the University of North Florida was supported by the Donors of the American Chemical Society Petroleum Research Fund PRF40209-B5M and by the National Science Foundation Grant No. DMR-03-05653. They also acknowledge S. Tsoi for stimulating discussions.

[1] The simplicity of the ground state of Mn^{2+} in the crystal field arises from the fact that the orbital state is an S state ($L=0$) so that the sixfold ${}^6S_{5/2}$ level splitting into Γ_8 and Γ_7 levels in a T_d field results from spin-orbit coupling mixing higher states in fourth order of perturbation theory. Thus, the $\Gamma_7-\Gamma_8$ energy splitting is extremely small.

[2] *Diluted Magnetic Semiconductors*, Semiconductors and Semimetals, Vol. 25 edited by volume editors J. K. Furdyna and J. Kossut and series editors R. K. Willardson and A. C. Beer (Academic, San Diego, 1988); J. K. Furdyna, J. Appl. Phys. **64**, R29 (1988).

[3] H. Alawadhi, I. Miotkowski, V. Souw, M. McElfresh, A. K. Ramdas, and S. Miotkowska, Phys. Rev. B **63**, 155201 (2001).

[4] S. Tsoi, I. Miotkowski, S. Rodriguez, A. K. Ramdas, H. Alawadhi, and T. M. Pekarek, Phys. Rev. B **69**, 035209 (2004).

[5] J. H. van Vleck, *The Theory of Electric and Magnetic Susceptibilities* (Oxford University Press, London, 1932).

[6] M. Villeret, S. Rodriguez, and E. Kartheuser, Physica B **162**, 89 (1990).

[7] M. Villeret, S. Rodriguez, and E. Kartheuser, Phys. Rev. B **43**, 3443 (1991).

[8] A. Mauger, D. Scalbert, J. A. Gaj, J. Cernogora, and C. Benoit à la Guillaume, Phys. Rev. B **43**, 7102 (1991).

[9] Y. Y. Zhou and C. Rudowicz, J. Magn. Magn. Mater. **163**, 80 (1996).

[10] J. P. Mahoney, C. C. Lin, W. H. Brumage, and F. Dorman, J. Chem. Phys. **53**, 4286 (1970).

[11] M. Hausenblas, L. M. Claessen, A. Wittlin, and A. Twardowski, Solid State Commun. **72**, 253 (1989).

[12] G. A. Slack, S. Roberts, and J. T. Vallin, Phys. Rev. **187**, 511 (1969).

[13] G. A. Slack, S. Roberts, and F. S. Ham, Phys. Rev. **155**, 170 (1967).

[14] D. Scalbert, J. Cernogora, A. Mauger, and C. Benoit à la Guillaume, Solid State Commun. **69**, 453 (1989).

[15] A. Twardowski, D. Heiman, Y. Shapira, T. Q. Vu, and M. Demianiuk, Solid State Commun. **82**, 229 (1992).

[16] A. Twardowski, X. C. Liu, D. Heiman, Y. Shapira, R. Kershaw, K. Dwight, and A. Wold, Solid State Commun. **89**, 245 (1994).

[17] M. Jouanne, C. Testelin, C. Rigaux, and A. Mycielski, Solid State Commun. **83**, 1061 (1992).

[18] S. Tsoi, I. Miotkowski, S. Rodriguez, A. K. Ramdas, H. Alawadhi, and T. M. Pekarek, Phys. Rev. B **72**, 155207 (2005).

[19] D. L. Peterson, A. Petrou, W. Giriat, A. K. Ramdas, and S. Rodriguez, Phys. Rev. B **33**, 1160 (1986).

[20] C. Testelin, C. Rigaux, A. Mauger, A. Mycielski, and M. Guillot, Phys. Rev. B **46**, 2193 (1992).

[21] D. Heiman, A. Petrou, S. H. Bloom, Y. Shapira, E. D. Isaacs, and W. Giriat, Phys. Rev. Lett. **60**, 1876 (1988).

[22] D. Scalbert, J. A. Gaj, A. Mauger, J. Cernogora, and C. Benoit à la Guillaume, Phys. Rev. Lett. **62**, 2865 (1989).

[23] C. Testelin, J. B. Prost, M. Menant, M. Zielinski, and A. Mycielski, Solid State Commun. **113**, 695 (2000); W. Mac, M. Herbich, Nguyen The Khoi, A. Twardowski, Y. Shapira, and M. Demianiuk, Phys. Rev. B **53**, 9532 (1996).

[24] Chee-Leung Mak, R. Sooryakumar, B. T. Jonker, and G. A. Prinz, Phys. Rev. B **45**, 3344 (1992).

[25] S. Venugopalan, A. Petrou, R. R. Galazka, A. K. Ramdas, and S. Rodriguez, Phys. Rev. B **25**, 2681 (1982).

[26] J. M. Baranowski, J. W. Allen, and G. L. Pearson, Phys. Rev. **160**, 627 (1967). There are two states in the ${}^5\Gamma_5$ multiplet of Γ_5 symmetry and are therefore final states allowed for electric dipole transitions originating from the Γ_1 ground state. The lower one has energy $\Delta+3\lambda+[18\lambda^2/(5\Delta)]+(24\lambda^2/\Delta)(1+2\lambda/\Delta)$ above Γ_1, with a value of 2486 cm^{-1} calculated using $\Delta=2693$ cm^{-1} and $\lambda=-102.2$ cm^{-1}. This transition gives rise to a sharp line. The other $\Gamma_1\rightarrow\Gamma_5$ transition with a final state in the upper multiplet corresponds to energy $\Delta-2\lambda+[12\lambda^2/(5\Delta)]+(24\lambda^2/\Delta)(1+2\lambda/\Delta)=2993$ cm^{-1}, a value in good agreement with 2990 cm^{-1} calculated using the complete 25-fold ${}^5D$ term. However, this second line is very broad and was not used in the present paper to obtain the values of Δ and λ used in this work.

[27] A. K. Bhattacharjee and S. Rodriguez, Phys. Rev. B **6**, 3836 (1972).

[28] Yasuo Oka and Manuel Cardona, Phys. Rev. B **23**, 4129 (1981).

[29] F. C. von der Lage and H. Bethe, Phys. Rev. **71**, 612 (1947).

[30] D. Colignon, E. Kartheuser, S. Rodriguez, and M. Villeret, Phys. Rev. B **51**, 4849 (1995).

[31] A. Twardowski, P. Glód, W. J. M. de Jonge, and M. Demianiuk, Solid State Commun. **64**, 63 (1987); A. Twardowski, P. Glod, P. Pernambuco-Wise, J. E. Crow, and M. Demianiuk, Phys. Rev. B **46**, 7537 (1992).

[32] A. Twardowski, K. Pakula, M. Arciszewska, and A. Mycielski, Solid State Commun. **73**, 601 (1990); A. Twardowski, K. Pakula, I. Perez, P. Wise, and J. E. Crow, Phys. Rev. B **42**, 7567 (1990).

[33] C. Testelin, C. Rigaux, A. Mycielski, and M. Menant, Solid State Commun. **78**, 659 (1991).

[34] M. Nawrocki, R. Planel, G. Fishman, and R. Galazka, Phys. Rev. Lett. **46**, 735 (1981).

[35] T. Dietl and J. Spalek, Phys. Rev. Lett. **48**, 355 (1982).

[36] T. Dietl and J. Spalek, Phys. Rev. B **28**, 1548 (1983).

[37] D. Heiman, P. A. Wolff, and J. Warnock, Phys. Rev. B **27**, 4848 (1983).

[38] D. L. Peterson, D. U. Bartholomew, U. Debska, A. K. Ramdas, and S. Rodriguez, Phys. Rev. B **32**, 323 (1985).

[39] C. Testelin, A. Mauger, C. Rigaux, M. Guillot, and A. Mycielski, Solid State Commun. **71**, 923 (1989).

[40] M. J. Seong, H. Alawadhi, I. Miotkowski, A. K. Ramdas, and S. Miotkowska, Phys. Rev. B **63**, 125208 (2001).